Effects of cerium addition on the microstructure, mechanical properties and strain hardening behaviour of TWIP steel Fe-18Mn-0.6c

ZHONG, Lingqiang, WANG, Zhigang, LUO, Quanshun <http://orcid.org/0000-0003-4102-2129> and LIU, Weizhen

Effects of cerium addition on the microstructure, mechanical properties and strain hardening behaviour of TWIP steel Fe-18Mn-0.6C

Lingqiang Zhong[a], Zhigang Wang [a,b,*], Quanshun Luo [c,**], Weizhen Liu [a]

a Faculty of Materials Metallurgy and Chemistry, Jiangxi University of Science and Technology, Ganzhou 341000, China
b National Rare Earth Functional Materials Innovation Center, Ganzhou 341000, China
c Materials and Engineering Research Institute, Sheffield Hallam University, Howard Street, Sheffield S1 1WB, UK
* Corresponding author at: Faculty of Materials Metallurgy and Chemistry, Jiangxi University of Science and Technology, Ganzhou 341000, China.
** Corresponding author.

ABSTRACT

The effects of cerium (Ce) on the microstructure, mechanical properties and strain hardening behaviour of Fe-18Mn-0.6C twin-induced plasticity (TWIP) steel were investigated by electron backscatter diffraction, X-ray diffraction and transmission electron microscopy. Compared with the addition of Al, the addition of Ce significantly reduced the stacking fault energy of TWIP steel, which promotes the formation of deformation and annealing twins. The dynamic strain aging behaviour of TWIP steel was inhibited by Al and Ce atoms during plastic deformation. The optimal mechanical properties were obtained when 0.015 wt% of Ce was added, resulting in a tensile strength of 1023 MPa; and an elongation was 92%. The interaction of twin variants in the Ce-containing alloys exhibited an X shape, which was significantly different from the T shape in the non-Ce containing alloy. This is mainly attributed to the fact that Ce promotes dislocations near grain boundaries, where for the nucleation of deformation twins at grain boundaries is favoured. Compared with the T-shaped twin variants, the dynamic Hall-Petch effect caused by the X-shaped staggered twin variants was stronger, which improved the strain hardening ability of TWIP steel.

Keywords: TWIP steel; Deformation twin interaction; Strain hardening; Stacking fault; Mechanical properties; Cerium

1. Introduction

Based on the comprehensive consideration of reducing energy consumption and improving safety performance, lightweight materials are becoming more prominent in the automobile industry. Twinning induced plasticity (TWIP) steel has excellent strength, plasticity and energy absorption, which makes it a good material for the structural parts of automobiles and anticollision parts [1,2]. The microstructure of TWIP steel is a single γ phase, and its excellent ductility is attributed to the strain hardening effect during plastic deformation [3]. It is widely accepted that the outstanding strain hardening capacity of TWIP steels mainly results from deformation twins and their interaction with dislocations [4]. McCormack [5] argued that the strain hardening effect caused by deformation twins can be divided into two parts: one part changes the dislocation accumulation rate, and the other part hardens the slip system directly through the Hall-Petch effect. The occurrence of deformation twinning can indirectly influence the evolution of the dislocation density. In addition, Bouaziz [6] et al. identified that back stress is an important mechanism of strain hardening. The back stress is generated by pile-ups of dislocations arrested at twin boundaries.

The stacking fault energy (SFE) of TWIP steel is the key parameter for twinning, and which the SFE depends on the composition and temperature [7,8]. The TWIP effect is triggered at low SFE values (20–40 mJ/ m^2) [9,10]. The SFE influences the processes of dislocation cross-slip and climb, which play an important role in the strain hardening behaviour of steel [11]. A low SFE value results in wide stacking faults, thus making dislocation cross-slip more difficult. It is worth noting that an SFE that is too low can lead to the formation of α'-martensite and reduce ductility. In other words, the SFE of TWIP steel can be adjusted to further promote the TWIP effect by adding alloying elements [12–14]. It is well known that Al and Cu additions increase the SFE, thereby resulting

in a decrease in the formation of deformation twins and finally decreasing the strain hardening capacity [15]. Kalsar et al. [16] reported that Ni improved twin activity, which increased the elongation of TWIP steel.

Although TWIP steel has high tensile strength and ductility, its shortcomings, such as low yield strength and delayed cracking, limit its practical application. Many efforts to overcome these disadvantages have been conducted using various other alloying elements, such as Al, Cu, and Si [17–20]. Elements such as Al and Cu generally reduce the ensile strength or toughness of TWIP steels because they inhibit the formation of deformation twins. Rare earth cerium (Ce) has attracted the attention of many researchers because the addition of Ce has been considered to improve the mechanical properties of austenite steels. Ce dissolved into the matrix, leading to solution strengthening and a Cottrell atmosphere, and increasing the yield strength. Moreover, Ce can improve the microstructure uniformity and the proportion of high angle grain boundaries, thus improving the total elongation [21]. Ce reduces the mismatch in hardness between ferrite and austenite, and this result suggests that Ce can improve the hot workability of steels consisting of ferrite and austenite [22]. Rare earth oxide could be the most effective heterogeneous nuclei of primary austenite and refine the primary austenite grain [23]. However, there is a lack of investigations regarding the strain hardening behaviour of TWIP steels containing Ce elements.

Therefore, the present work addresses the influence of Ce on the mechanical properties of TWIP steels to promote the TWIP effect and improve the yield strength. Dynamic strain aging (DSA) and delayed cracking were strongly inhibited by the addition of Al. Two commonly used components of the second generation of high manganese TWIP steel, namely, Fe-18Mn-0.6C and Fe-18Mn-0.6C-1.5Al, and the alloy obtained by adding Ce to the matrix composition of Fe-18Mn-0.6C were studied. The addition of Al has been studied as an element to improve the SFE [24]. The effects of Ce on the strain hardening behaviours, microstructure and mechanical properties of the alloy are discussed.

2. Material and methods

Four grade 20 kg ingots with different Ce and Al contents were prepared by vacuum induction melting. The analysed chemical compositions are listed in Table 1. Ce was measured by the inductively coupled plasma method (PlasmaQuant MS). Mn and Al element were measured by a direct-reading spectrometer (FOUNDRY-MASTER Xline). The contents of C element were measured by infrared carbon and sulphur analyser (CS-3000G). For convenience, these four steels are referred to as '0Ce', '0.015Ce', '0.045Ce', and '1Al' hereafter. The ingots were heated to 1100 ◦C for 30 min before forging. The initial forging temperature is 1100 ◦C, and the finish forging temperature is 800 ◦C. The ingots with a thickness of 30 mm are soaked at 1200 ◦C for 2 h to reduce the segregation of alloying elements, and then they are hot-rolled to a final thickness of 4.5 mm with a thickness reduction per pass of 30% and a total thickness reduction of 85% without intermediate reheating. The starting and finishing temperatures of hot rolling are approximately 1150 ◦C and 850 ◦C, respectively, followed by air cooling to room temperature.

Table 1
Chemical compositions of the experimental steels.

Steel	Elements(wt%)				
	Mn	C	Ce	Al	Fe
0Ce	17.13	0.68	<0.01	<0.01	Bal.
0.015Ce	17.64	0.63	0.015	<0.01	Bal.
0.045Ce	16.80	0.63	0.045	<0.01	Bal.
1Al	17.22	0.62	<0.01	1.00	Bal.

Dumbbell-type tensile specimens having a gauge length of 50 mm, 12.5 mm (width) and 3 mm (thickness) were prepared along the direction of hot rolling. Uniaxial tensile testing at room temperature is performed on a UTM 5150 universal tensile testing machine with a strain rate of 5 × 10- 4 s- 1. Before testing, the surface of each specimen was mechanically polished.

Electron back-scatter diffraction (EBSD) measurements were conducted using a Sigma Scanning electron microscope (SEM) equipped with a EBSD system at 15 kV and a sample tilt angle of 70◦. The microstructure of hot rolled and deformed samples was analysed by scanning spatial step sizes of 1 μm and 150 nm, respectively. Conventional polishing was performed with a solution of 10% HClO4 + 20% glycerol +70% CH3CH2OH under a potential of 20 V. Channel 5 software was used for data collection and analysis. Twin boundaries (TBs) were defined as Σ3 = 60◦〈111〉 [4]. To measure the local misorientation, the kernel average misorientation (KAM) value was calculated up to the 3rd nearest-neighbour shell with a maximum misorientation angle of 5◦.

Microscopic analyses after tensile tests were performed using an FEI Talos F200X transmission electron microscope (TEM). Thin foils for TEM observations were all sliced from the gauge by spark cutting and then

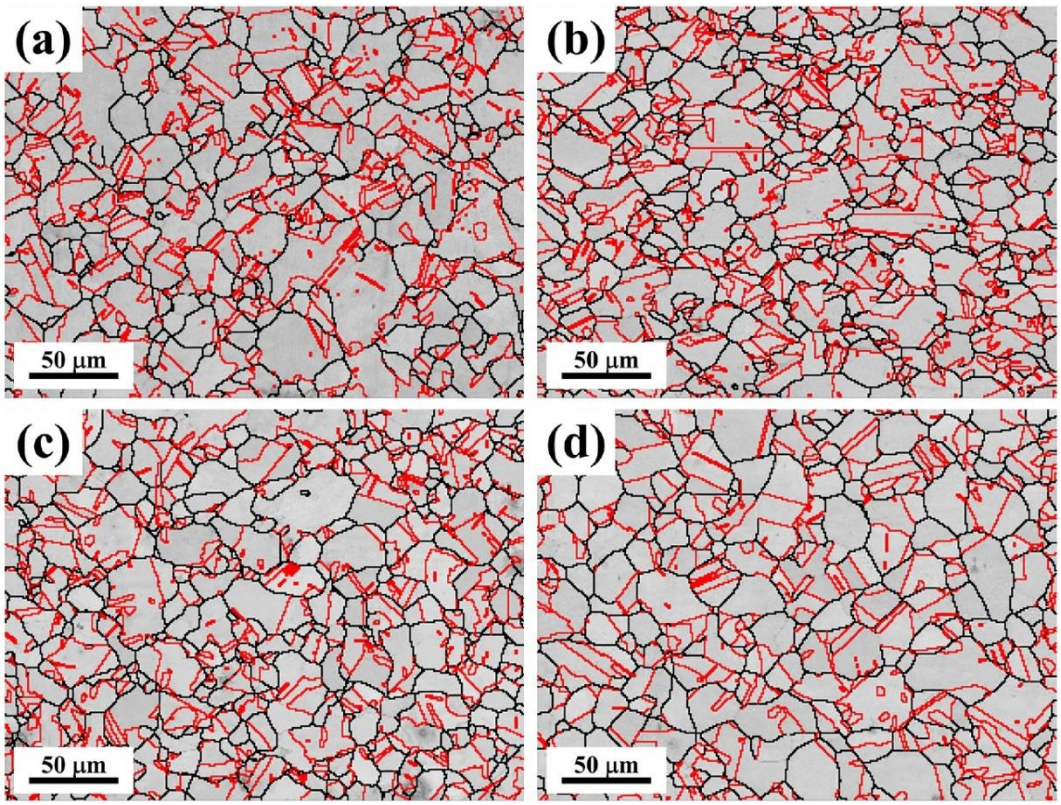

Fig. 1. EBSD boundary map of steels. (a) 0Ce; (b) 0.015Ce; (c) 0.045Ce and (d) 1Al. (the black and red lines correspond to the high-angle grain boundaries($\theta > 15^\circ$) and Σ3 twin boundaries, respectively. The tolerance angle was 5◦ for twin fraction calculation.) (For interpretation of the references to colour in this figure legend, the reader is referred to the web version of this article.)

mechanically thinned to a thickness of 100 μm, followed by ion-beam milling in a Gatan691 precision ion polishing system (PIPS) at 5 kV. Finally, conventional twin-jet polishing with a solution of 10% HClO4 + 90% CH3CH2OH under a potential of 40 V at - 30 ◦C was performed.

To examine the constituent phases of the specimen and stacking fault, a Rigaku D/max 2550 VB/PC X-ray diffractometer was used with Cu Kα radiation (λ = 0.154056 nm) operated at 40 kV at room temperature. The scanning range (2θ) and step size were 40–100◦ and 0.02◦, respectively. The XRD patterns were analysed by TOPAS software. The stacking fault probability (Psf) was determined by the peak-broadening method, for which the basic equations are as follows [25–27]:

$$P_{sf} = \frac{a}{1-\frac{\sqrt{3}}{4}}\left[\left(\frac{1}{D_{eff}}\right)_{200} - \left(\frac{1}{D_{eff}}\right)_{111}\right] \quad (1)$$

$$D_{eff} = \frac{\lambda}{\beta_0 cos\theta} \quad (2)$$

β0 is the essential integrated width, Deff is the mean effective crystallite size, b0 is the instrumental integrated width, and a is the lattice constant. To verify the accuracy of the calculation of Psf, the following two equations of integral breadth relations were used to calculate β0:

$$B_0^2 = \beta_0^2 + b_0^2 \quad (3)$$

Eq. (3) is the integral width relation, from which the value of B0 can be determined, where B0 is the measurement integrated width. b0 is the instrumental integrated width.

3. Results

The microstructure of hot rolled steels consisting of fully recrystallized grains, including annealing twins, was observed, as shown in Fig. 1a-d. To analyse the influence of Ce and Al on the distribution of twins, the grain size and twin volume fraction of different samples were counted, as shown in Fig. 2, and the data were the average values of the two test results. The twin volume fraction is defined as the area of annealing twins per observed area [6,20,28,29]. An increase in the twin volume fraction with the addition of Ce was observed. However, the twin

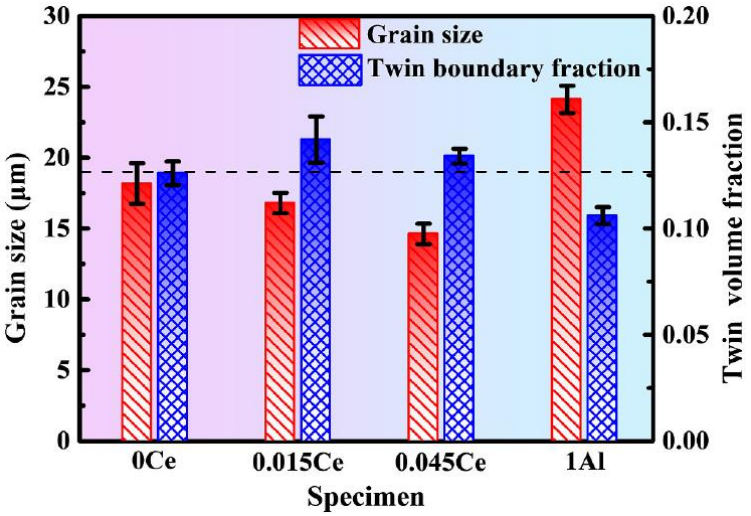

Fig. 2. Grain size and twin volume fraction of steels.

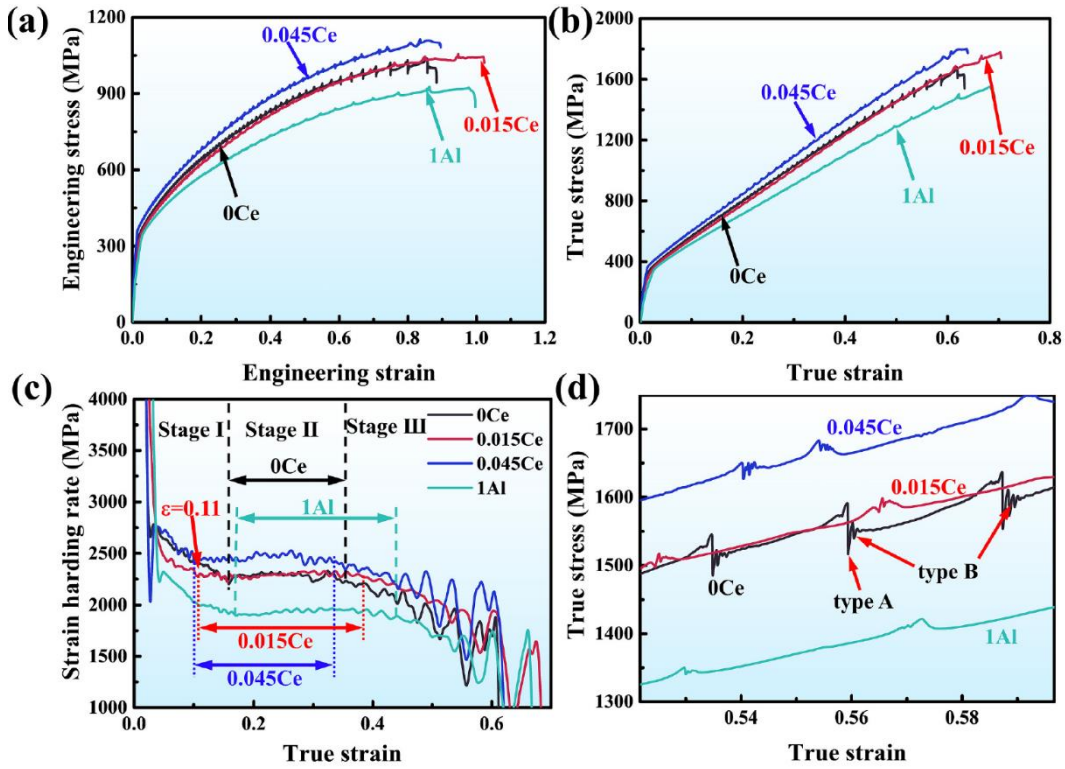

Fig. 3. Mechanical properties and serration flow phenomena of TWIP steels. (a) Engineering stress-strain curves; (b) True stress-strain curves; (c) Strain-hardening rate curves; and (d)Serrated flow phenomena.

volume fraction was significantly reduced after Al addition. The grain size decreased with an increase in Ce content. With the addition of 1% Al, the increase in the grain size was approximately 6 μm on average. Annealing twins can enhance the strength by blocking dislocation movement during plastic deformation. A higher density of annealing twins yields a higher strength [30].

Fig. 3a shows the tensile engineering stress versus strain curves of the alloys at room temperature (298 K). The tensile properties of the alloys are listed in Table 2. As shown in Fig. 3a, all the steels exhibited continuous yielding behaviour. The yield strength (YS) and ultimate tensile strength (UTS) of 0.045Ce are the highest, reaching averages of 385 MPa and 1107 MPa, respectively. The increase in yield strength was mainly attributed to the decrease in grain size. Zhao et al. [21] also reported that the addition of 0.02 wt% Ce improved the yield strength of Fe-Mn-C-Al TWIP steel. Although the grain size of the 1Al sample was largest, the lattice friction increased due to the solution strengthening effect of Al, so the yield strength of the 1Al sample did not decrease compared with that of 0Ce. The 0.015Ce and 1Al showed a high total elongation (TE). The product of ultimate tensile strengths and total elongation (UTS*TE) indicates the energy absorption capacity of TWIP steels. The

Table 2
Mechanical properties of the experimental steels.

Alloy	YS (MPa)	UTS (MPa)	TE (%)	UTS*TE (GPa*%)
0Ce	363 ± 4	1019 ± 13	79.4 ± 3.1	81.4 ± 3.7
0.015Ce	362 ± 3	1023 ± 18	92.0 ± 2.5	95.8 ± 4.2
0.045Ce	385 ± 6	1107 ± 12	79.6 ± 4.5	88.2 ± 5.9
1Al	360 ± 4	920 ± 6	91.2 ± 2.7	83.9 ± 3.0

UTS*TE of 0.015Ce and 0.045Ce steel is 95.8 and 88.2 GPa*%, respectively, which was higher than that of 0Ce (81.4 GPa*%) and 1Al (83.9 GPa*%). The tensile test results showed that the addition of Ce increased the energy absorption capacity of TWIP steel.

The true stress-strain curve and strain hardening rate curve were drawn from the engineering stress-strain curve, as shown in Fig. 3b and c. TWIP steel with added Ce exhibited a higher maximum true stress, and the maximum true stresses of 0.015Ce and 0.045Ce were almost the same, both of which were 1786 MPa, while that of 0Ce was 1643 MPa. The strain hardening stage of the sample was divided into stages I, II and III. Stage II maintained a constant strain hardening rate. Sample 0.045Ce was the first to initiate stage II, and 1Al was the last. Additionally, 0.045Ce had the highest strain hardening rate at stage II. The tensile strength decreased significantly after the addition of Al, which was mainly attributed to the decrease in the work hardening capacity.

Plastic instability gives rise to serrations in the stress-strain curves and the simultaneous localization of deformation in the specimens. The serrated flow on the tensile curves is generated by DSA, as shown in Fig. 3d. According to the research of Jacobs et al. [31], the serrated flow on the true stress-strain curve of 0Ce steel can be divided into Type A (periodic serrations) and Type B (oscillation serrations), which contributes to the interaction between solid solution atom C and movable dislocation. As shown in Fig. 3b, the addition of 0.015% Ce and 1% Al can effectively weaken the DSA, which is conducive to improving the plasticity of TWIP steel [32,33]. Additionally, surface wrinkle defects of TWIP steel were prevented in the processing process. Moreover, Fig. 3d shows that the serrated flow of the addition of both Ce and Al transitions from the A + B type to type A. This was related to the improvement in C diffusion activation energy from Ce and Al atoms. Lee et al. [34] proposed that a single diffusive hop (reorientation) of the C atom in the CMn complex causes DSA by interacting with stacking faults. Al increases the SFE and reduces the C diffusivity in austenite. Al suppresses the C- vacancy short-range clustering or the jumps to tetrahedral sites [35,36]. However, there is no detailed information on the effect of Ce addition on the DSA phenomenon in TWIP steels. The weakening of DSA may be related to the lattice distortion caused by the solution of Ce atoms pinning C atoms [37] and inhibiting the reorientation of C atoms.

To explore the different twin behaviours of the four TWIP steels with tensile strain, the microstructure evolution was determined by EBSD. Fig. 4a-d shows the band contrast and twin boundary images at a true strain of 0.12 ($\varepsilon = 0.12$). Blue lines inside the grains contain nanoscale deformation twins and wider annealing twins. As shown in Fig. 4a-c, with increasing Ce content, the deformation twins inside the grains increased. However, it is difficult to find deformation twins in 1Al, as shown in Fig. 4d.

To understand the distribution of intragranular local misorientation, the KAM maps of the four alloys at $\varepsilon = 0.12$ were measured, as shown in Fig. 5. The misorientation with respect to the first nearest-neighbour approximation is presented here. The regions with higher KAM values are concentrated around the grain boundaries. With increasing Ce content, this phenomenon becomes more significant, as shown in Fig. 5a-c. A high KAM value indicates a large strain and dislocation density in this region; in other words, there is high stress in this region.

Because the twinning nucleation stress is higher than the dislocation slip stress, the local stress concentration provides beneficial conditions for twinning nucleation [38]. It is worth noting that the distribution of KAM in the 1Al alloy was extremely uniform, as shown in Fig. 5d. This indicates that deformation is uniformly developed in the 1Al alloy, which is one of the reasons why the formation of deformation twins does not occur easily in the sample. Plasticity is also improved as a result.

Fig. 6(a)-(c) shows the band contrast maps and twin boundary maps at a strain of 0.2 and the corresponding twin boundaries. Twin bundles began to appear at 0.015Ce and especially in 0.045Ce. In addition, twin interactions between twin variants occurred in most grains of 0.045Ce but are difficult to observe in 0Ce.

Fig. 7 shows the IPF and band contrast maps from the 0Ce and 0.045Ce strained tensile samples at $\varepsilon = 0.43$. The activation of twin systems is observed with a significant number of grains for the two samples. With increased twin density, sub-boundaries developed within the grains that delimited different twin bundles. According to Fig. 7(a) and (b), most deformation twin orientations were 〈001〉//TA. Compared with 0Ce, 0.045Ce formed more twinning bundles. Fig. 8 shows the HRTEM maps and fast Fourier transformation (FFT) spots of twin bundles in 0.045Ce. In Fig. 8(a), twin interfaces are marked by yellow arrows. Many twins are packed together, and the boundaries are so close together that they are only a few atomic layers thick. Fig. 8(b)-(e) show the FFTs

corresponding to the four regions with twin interfaces in Fig. 8 (a). Multiple twins were confirmed by the selected area diffraction pattern. The two sets of electron diffraction patterns in the matrix and twin parts of the adjacent FFT patterns are in opposite positions (the circled spots are diffraction spots of twins). This proves the existence of twin bundles which are shown in Fig. 7. In addition, this also indicates that the existing twin interface can be used as the twin surface of the newly formed twins. Twins in a twin bundle are almost completely connected. The deformation twins in TWIP steel are initially very thin, and the thickness does not increase substantially with increasing strain. The growth of the volume fraction of twins is mostly furnished by the formation of new twins

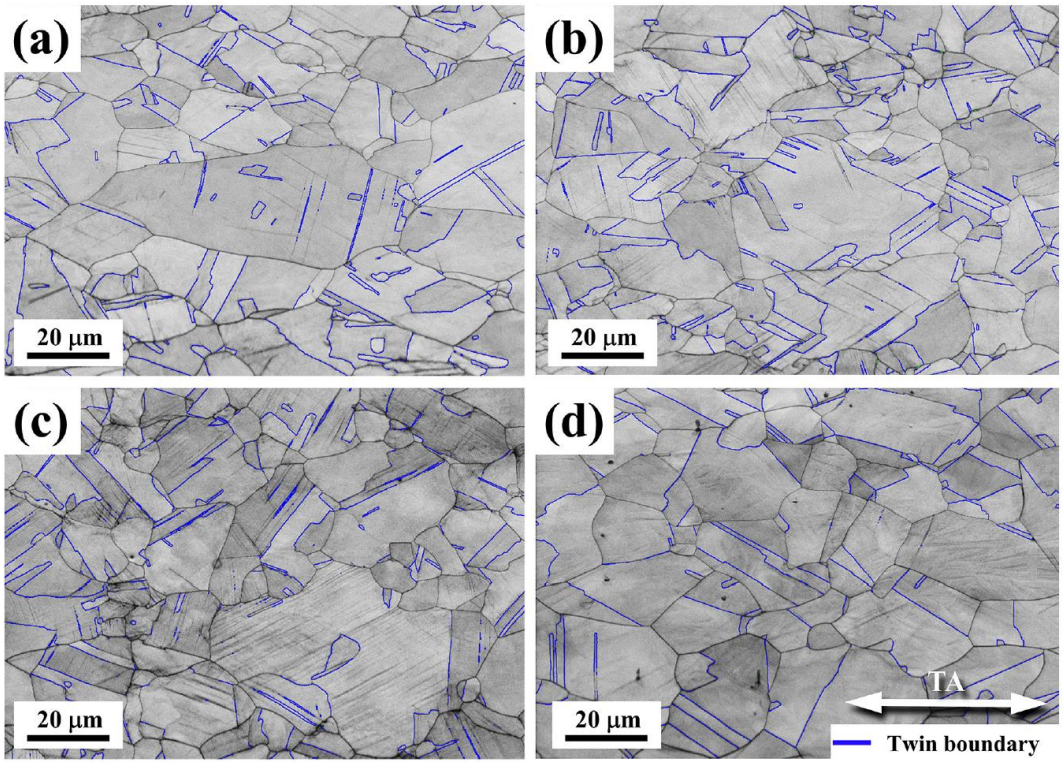

Fig. 4. Band contrast maps and twin boundary maps for steels at ε = 0.12. (a) 0Ce; (b) 0.015Ce; (c) 0.045Ce and (d) 1Al. (TA: tensile axis).

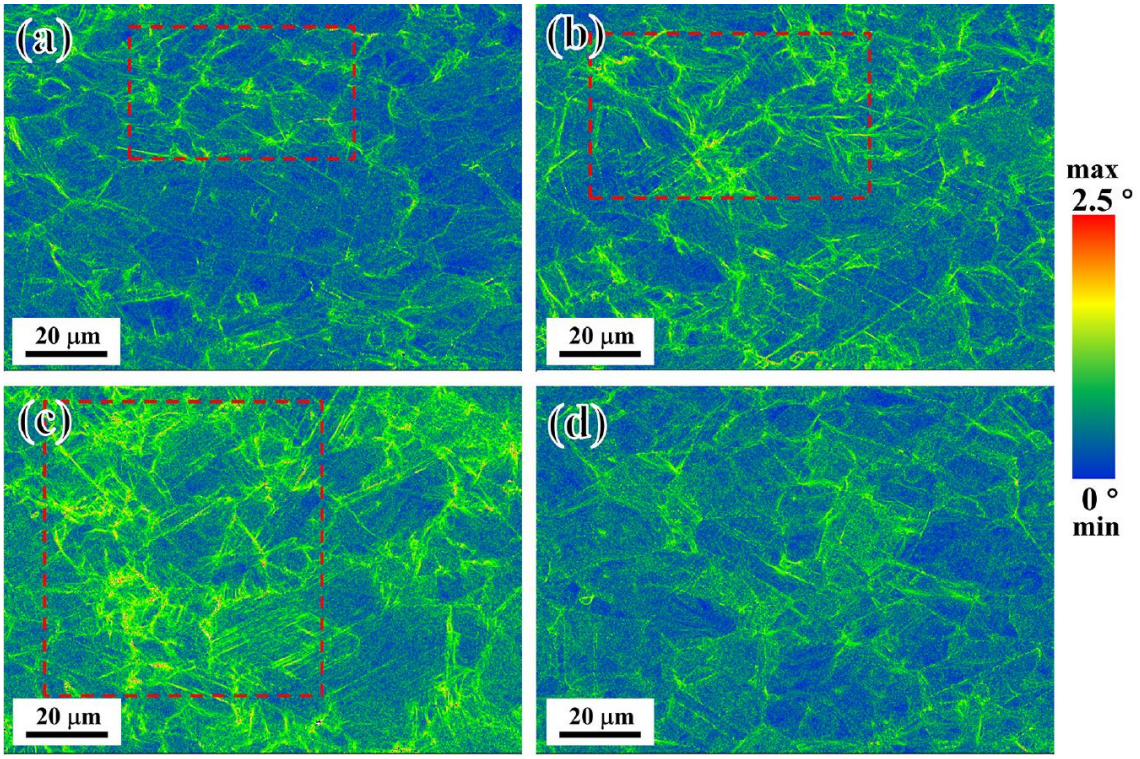

Fig. 5. KAM maps at ε = 0.12. (a) 0Ce; (b) 0.015Ce; (c) 0.045Ce and (d) 1Al.

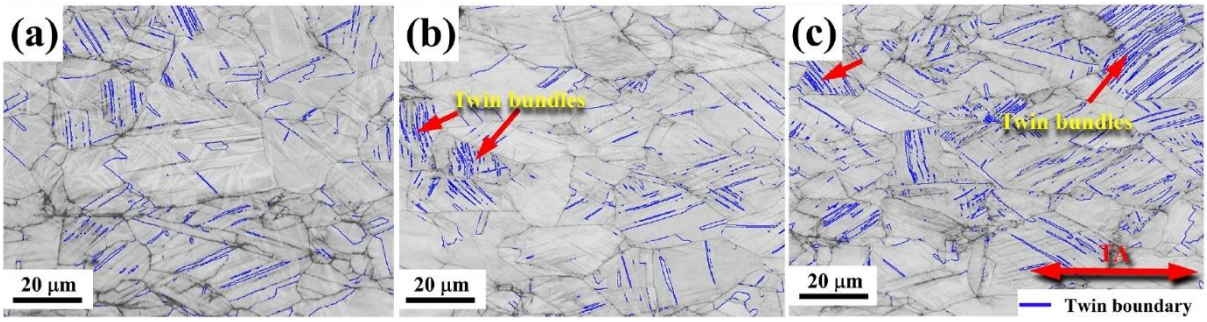

Fig. 6. Band contrast maps and twin boundary maps for steels at ε = 0.2. (a) 0Ce; (b) 0.015Ce; (c) 0.045Ce (TA: tensile axis).

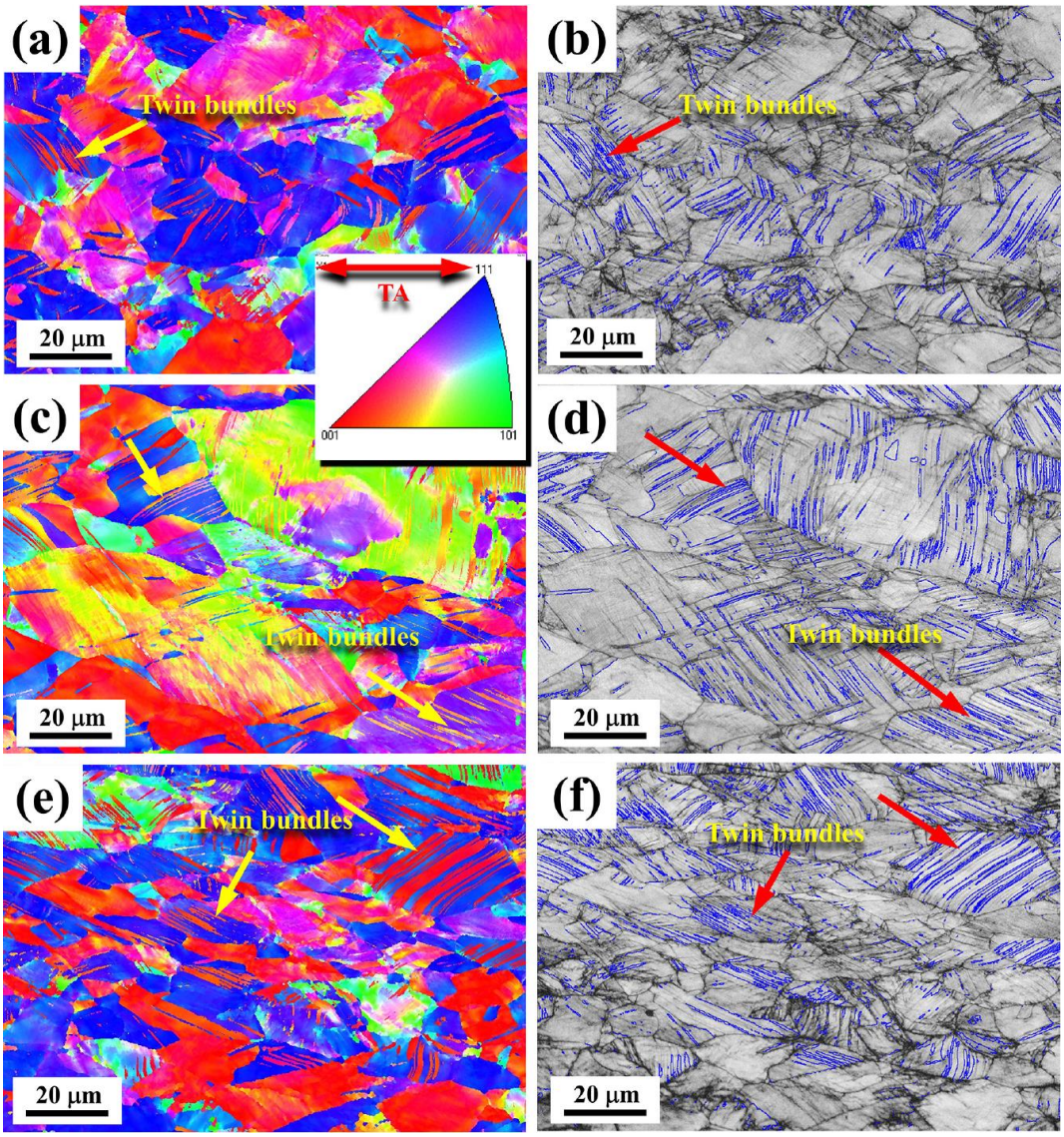

Fig. 7. Inverse pole figure (IPF) and band contrast maps from the 0Ce, 0.015Ce and 0.045Ce strained tensile samples at ε = 0.43. (a, b) 0Ce; (c, d) 0.015Ce; (e, f) 0.045Ce.

in the course of deformation. Ce may promote the formation of new twins due to the increase in Psf. This effectively explains why the twin density of 0.045Ce steel is higher than that of 0Ce steel, as shown in Fig. 7(c) and (d). TEM and EBSD observations support the finding that the addition of Ce promotes the formation of twins, including annealing twins and deformation twins.

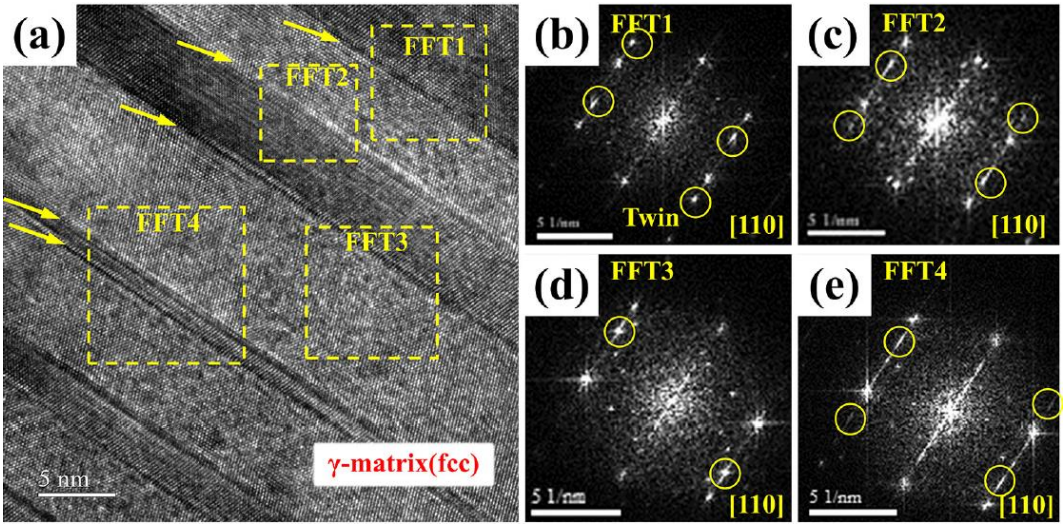

Fig. 8. HRTEM analyses of sample 0.045C at its straining state at ε = 0.43: (a) a phase-contrast lattice image showing twin bundles; (b-e) FFT patterns obtained in the specified areas. (Zone axis = [110]).

4. Discussion

Fig. 9a shows the X-ray diffraction patterns of the four TWIP steels. The figure shows the presence of only austenitic peaks. These steels were fully composed of the austenite phase. Fig. 9b and c show the peak shapes of the γ (111) and γ (200) peaks. The addition of Ce leads to the broadening of the two peaks, and 1Al exhibits the opposite trend. Based on the above equations, the Psf of the four steels is calculated, and the results are shown in Fig. 9d. As shown in the figure, with increasing Ce content, Psf increases, while the addition of Al reduces Psf. The study shows that Psf is inversely proportional to the SFE. Therefore, it can be concluded that the SFE of the sample decreases with increasing Ce content [26]. The SFE of the sample increased when Al was added. For the conclusion that Al improves the SFE of TWIP steel, many studies have obtained relatively similar theoretical and experimental data [39–41].

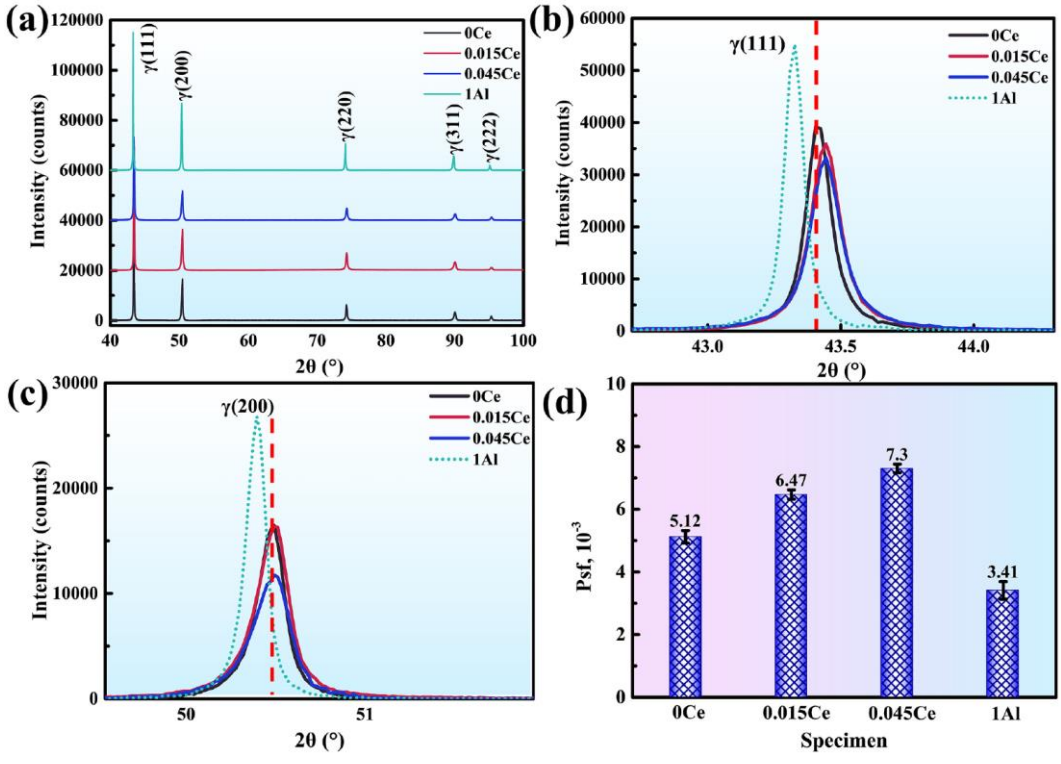

Fig. 9. (a) XRD patterns of the TWIP steels; (b) γ (111) peak; (c) γ (200) peak; (d) stacking fault probability of the TWIP steels.

Fig. 10 shows the TEM bright field (BF) images of the 0Ce and 0.045Ce specimens having a pre-strain of ε = 0.43. Many dislocation tangles can be found between the deformation twin boundaries. The presence of deformation twins could be confirmed by the diffraction spots of selected area diffraction (SAD). Stacking faults at the deformation twin interface were observed in 0Ce steel. Second twin variants were observed in 0.045Ce steel.

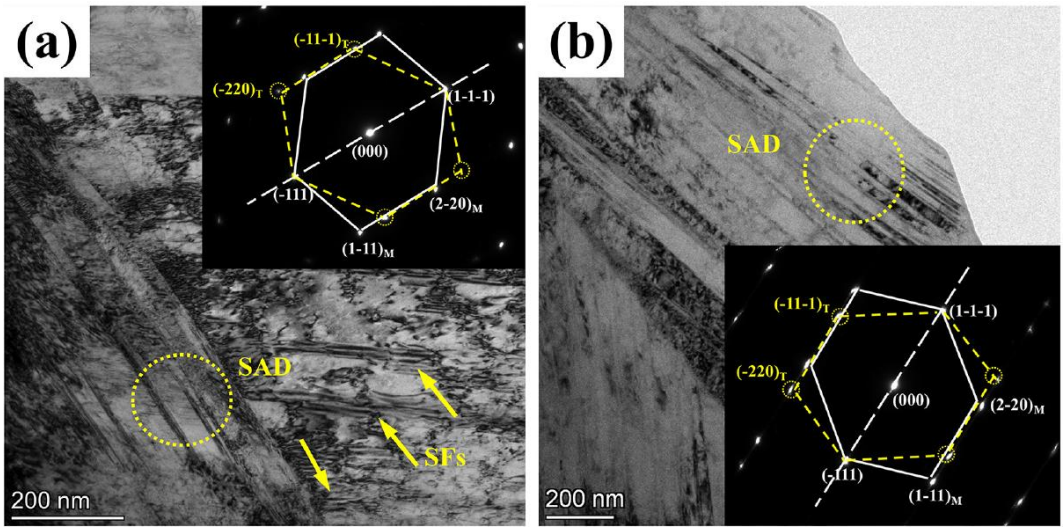

Fig. 10. TEM BF images and associated SAD analysis at ε = 0.43. (a) 0Ce; (b) 0.045Ce. (SFs: stacking faults; M: matrix; T: twin).

Fig. 11 shows the evolution of the twin fraction (The ratio of the high angle grain boundaries with the corrected Σ3 boundaries) of the three TWIP steels with tensile strain. The corrected Σ3 boundaries not include Σ3 annealing twin boundaries. The Σ3 twin fraction of all the TWIP steels initially increased with tensile strain curves. The difference in SFE due to Ce additions changed the curve of the twin fraction. A significant increase in twin volume fraction was observed in the 0.045Ce steel; therefore, this steel had a higher twin volume fraction at all strain levels. It also shows that the twinning rate of the 0.045Ce steel was the highest, especially at low strain levels (ε < 0.2).

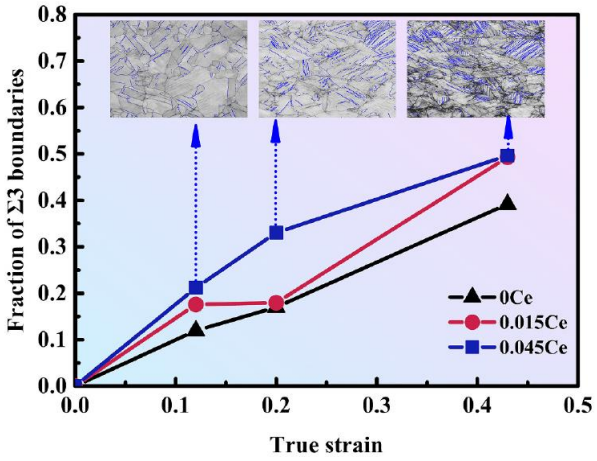

Fig. 11. Variation in fraction of Σ3 boundaries of the three TWIP steels with tensile strain. (The fraction means the ratio of the high angle grain boundaries with the corrected Σ3 boundaries).

In stage I, the dislocation activity and its interaction with the first twin variants are the main factors. The twins belonging to the first twin variant system are coplanar with the slip system, so the effect of the deformation twin on strain hardening was not significant in stage I. This stage is dominated by the dynamic recovery of dislocations, and the work hardening rate continues to decrease. When the strain is higher (ε > 0.12), as shown in stage II, the second twin variants occur [42]. Stage II is characterized by a progressively elevated or balanced strain hardening rate. The first twin variants are not coplanar with the second twin variants, and their interaction significantly affects the dynamic recovery of dislocations [43]. Therefore, the formation of noncoplanar twins significantly affects the strain hardening behaviour of TWIP steel. The initial strain of stage II is generally considered to be caused by the formation of noncoplanar twin variants [44]. As shown in Fig. 3, the starting strains of stage II for each steel are somewhat different. This is directly related to the SFE of the sample. A lower SFE can make the second twin variants appear earlier.

The twin morphology shown in Fig. 12(a), annealing twins and secondary twins formed in annealing twins, as well as deformation twins in second twin systems, can be observed for the 0Ce samples. The deformation twin density in the 0Ce sample is quite high, but there is no twin variants interaction with a staggered distribution, as shown in (b) and (c). As shown in Fig. 12(b), the staggered deformation twins divide the grains into smaller, independent regions. This not only makes the dynamic recovery of dislocations occur only in a small area, but also promotes the dynamic Hall-Petch effect. As shown in Fig. 12(c), the deformation twin density of 0.045Ce is higher than that of 0.015Ce, and the cross-distribution of deformation twins is also observed. Interestingly, the higher density and more variant system of twins of 0.045Ce are shown in Fig. 12(c).

The most likely scenario for the twin behaviour of the samples with different Ce contents is therefore described in Fig. 13. As shown in Fig. 13(a), deformation twins with a "T"-shaped distribution may be formed by stacking faults emitted from the deformation twins. Staggered deformation twins may be formed by stacking faults emitted from grain boundaries. Due to the reduction of the SFE in rare earth microalloying steels, rare earth elements cause an increase in the dislocation density and promote the formation of twins [45,46]. The main assumption of the model originally proposed by Olson and Cohen [47] is that a stacking fault in an fcc crystal structure is basically a thin layer of hexagonal close-packed (hcp) phase, separated from the matrix by a phase boundary on each side. The ideal stacking fault energy (γSFE) is then expressed by:

$$\gamma_{SFE} = 2\rho\Delta G^{\gamma\to\varepsilon} + 2\sigma \qquad (4)$$

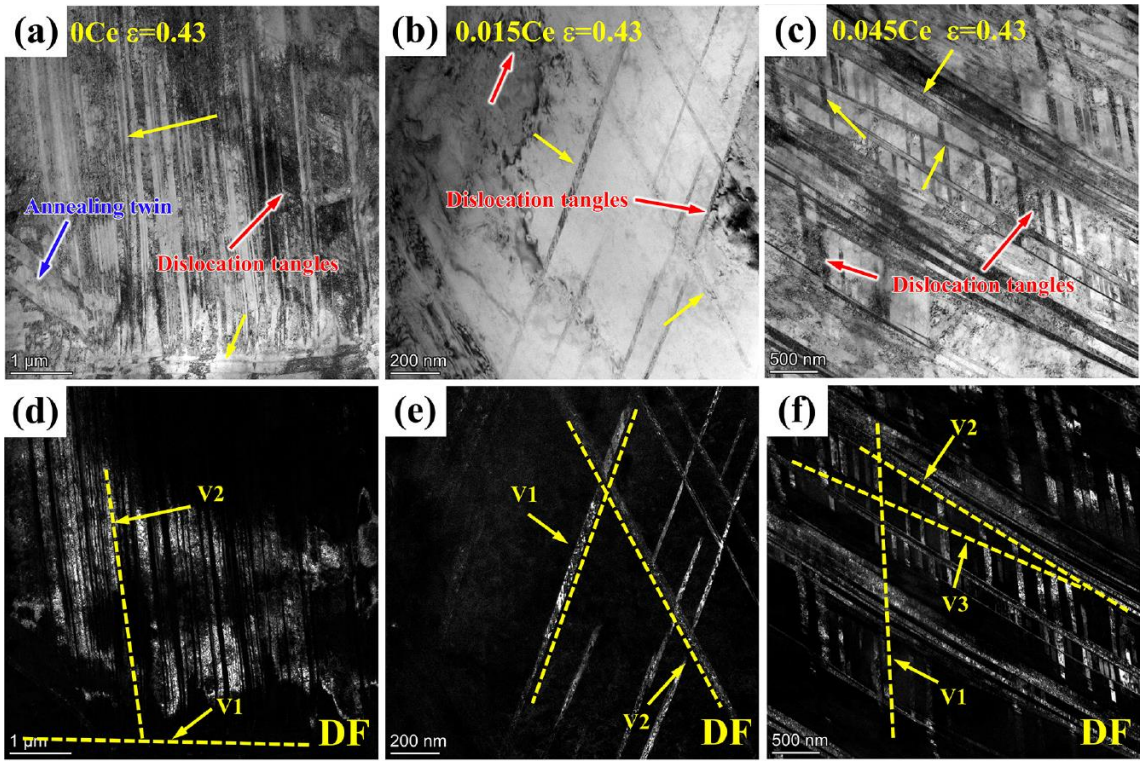

Fig. 12. TEM BF and DF images of steels at ε = 0.43. (a, d)0Ce; (b, e) 0.015Ce and (c, f) 0.045Ce. (V: twin variants).

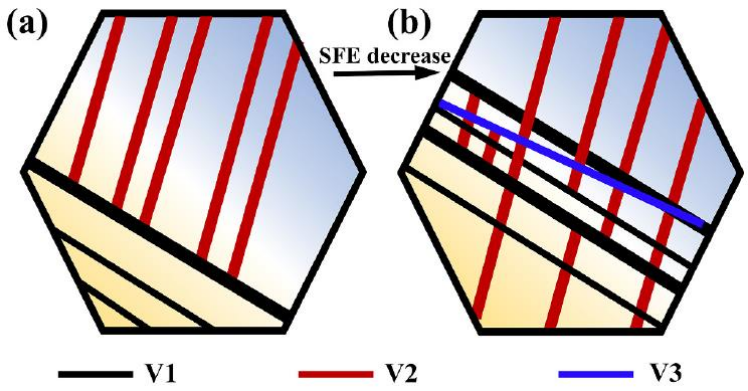

Fig. 13. Schematic diagram of the effect of the SFE on the deformation twin structure.

where ρ is the molar surface density along planes, $\Delta G^{\gamma \rightarrow \varepsilon}$ is the molar Gibbs energy of the austenite to ε-martensite phase transformation $\gamma\text{-}fcc \rightarrow \varepsilon_{hcp}^{Ms}$ and σ is the interfacial energy per unit area of the phase boundary. Researchers have indicated that Ce significantly affects the austenite to ε-martensite phase transformation [48,49]. This is favorable evidence that Ce influenced $\Delta G^{\gamma \rightarrow \varepsilon}$. This evidence also shows that Ce can affect the SFE.

Moreover, it has also been reported that at a high strain state, the twinning activity is controlled by the local stress state instead of simply grain orientation, because the local stress state may be very different from the macroscopic stress state [38]. Based on Fig. 5, we found that the addition of Ce also changed the local stress state. Ce promoted dislocations occur near grain boundaries, which provides favourable conditions for the nucleation of deformation twins at the grain boundaries.

With the addition of Ce, the lower the SFE is, the more easily deformation twins are generated. This is reflected in two aspects: firstly, the volume fraction of deformation twins will increase. Secondly, as SFE decreases, we find a third twinning variant, indicating that the third twinning system is activated. Only two twin variants are usually observed in TWIP steels (primary and secondary twin systems) [43]. The third twin system in TWIP steel exists and is activated by the reduction of SFE [50]. However, the ease with which twin systems can be activated varies with different grain orientations. Gutierrez et al. divided grains into three types according to grain orientation to distinguish twin substructures formed in different grains [43]. A study that further detailed examinations on single crystals are necessary, and we will discuss in the next step of this ongoing research.

When the deformation twins proliferate to a certain amount, they reach the saturation state, and the formation rate of deformation twins decreases greatly [3,6,20]. After deformation twin saturation, the work hardening rate of TWIP steel decreases rapidly until fracture. The formation rate of deformation twins at 0.045Ce is faster, so it is easier to reach saturation than at 0.015Ce. The strain hardening rate of 0.045Ce is reduced faster than that of 0.015Ce. This is why the plasticity of 0.045Ce is lower than that of 0.015Ce.

Grässel et al. [7] observed that large scale deformation twinning occurred in a TWIP steel when its Mn content was larger than 25%, the Al content was in excess of 3%, and the Si content was in the range of 2–3% (by weight). A very favourable strength-ductility balance was attained. An important quantity that characterizes this balance is the product of the ultimate tensile strength and the total elongation. The elongation of Fe-30Mn-3Al-3Si TWIP steel can reach more than 100%, but its strength is low (~600 MPa). An important direction for the development of TWIP steel is the balance of strength and plasticity. To achieve this goal, we change the twinning behaviour of TWIP steel and affect the work hardening behaviour in each plastic deformation stage by regulating the SFE by Ce microalloying. As shown in Fig. 11, 0.045Ce steel has a higher density of twins, which is conducive to improving its tensile strength. It achieves a better balance between strength and plasticity.

5. Conclusions

(1) Compared with the addition of Al, the addition of Ce increases the annealing twin volume fraction of TWIP steel. This is mainly attributed to Ce increasing the stacking fault probability of TWIP steel, while Al can significantly reduce it. Moreover, Ce promotes the formation of deformation twins, and the sample with higher Psf starts stage II earlier.

(2) Both Ce and Al can effectively weaken the DSA behaviour of TWIP steel when deformation occurs and make the serrated flow type change from Type A + B to Type A. When the addition of Ce is 0.015 wt%, the total elongation of TWIP steel is significantly improved, and it has excellent properties with a tensile strength of 1023 MPa and total elongation of 92%.

(3) The interaction mode between the twin variants is significantly influenced by Ce addition in TWIP steel. The twin variants interaction in the 0Ce samples tend to be T-shaped and tend to be X-shaped and staggered in the Ce-added samples. This result is mainly attributed to the Ce-promoted dislocation occurring near grain boundaries. Thus, the strain hardening ability of TWIP steel is improved by the addition of Ce.

Declaration of Competing Interest

The authors declare that they have no known competing financial interests or personal relationships that could have appeared to influence the work reported in this paper.

Acknowledgments

This work was supported by the Key Research and Development Program of Jiangxi Province (Grant No. 20192BBEL50016 and 20192ACB50010), and the Program of Qingjiang Excellent Young Talents, Jiangxi University of Science and Technology (JXUSTQJBJ2020007).

References

[1] M. Faccoli, G. Cornacchia, M. Gelfi, A. Panvini, R. Roberti, Notch ductility of steels for automotive components, Eng. Fract. Mech. 127 (2014) 181–193.

[2] E.D. Palma- Elvira, P. Garnica-Gonzalez, J.S. Pacheco-Cede˜no, J.J. Cruz Rivera, M. Ramos-Azpeitia, C.G. Garay-Reyes, J.L. Hernandez-Rivera, Microstructural development and mechanical properties during hot rolling and annealing of an automotive steel combining TRIP/TWIP effects, J. Alloys Compd. 798 (2019) 45–52.

[3] K. Renard, H. Idrissi, D. Schryvers, P.J. Jacques, On the stress state dependence of the twinning rate and work hardening in twinning-induced plasticity steels, Scr. Mater. 66 (2012) 966–971.

[4] D.R. Steinmetz, T. J¨apel, B. Wietbrock, P. Eisenlohr, I. Gutierrez-Urrutia, A. Saeed-Akbari, T. Hickel, F. Roters, D. Raabe, Revealing the strain-hardening behavior of twinning-induced plasticity steels: theory, simulations, experiments, Acta Mater. 61 (2013) 494–510.

[5] S.J. McCormack, W. Wen, E.V. Pereloma, C.N. Tom´e, A.A. Gazder, A.A. Saleh, On the first direct observation of de-twinning in a twinning-induced plasticity steel, Acta Mater. 156 (2018) 172–182.

[6] O. Bouaziz, S. Allain, C. Scott, Effect of grain and twin boundaries on the hardening mechanisms of twinning-induced plasticity steels, Scr. Mater. 58 (2008) 484–487.

[7] O. Gr¨assel, L. Krüger, G. Frommeyer, L.W. Meyer, High strength Fe-Mn-(Al, Si) TRIP/TWIP steels development - properties - application, Int. J. Plast. 16 (2000) 1391–1409.

[8] S.-J. Lee, Y.-K. Lee, A. Soon, The austenite/ε martensite interface: a first-principles investigation of the fcc Fe(111)/hcp Fe(0001) system, Appl. Surf. Sci. 258 (2012) 9977–9981.

[9] S. Allain, J.P. Chateau, O. Bouaziz, A physical model of the twinning-induced plasticity effect in a high manganese austenitic steel, Mater. Sci. Eng. A 387-389 (2004) 143–147.

[10] D.T. Pierce, J.A. Jim´enez, J. Bentley, D. Raabe, C. Oskay, J.E. Wittig, The influence of manganese content on the stacking fault and austenite/ε-martensite interfacial energies in Fe–Mn–(Al–Si) steels investigated by experiment and theory, Acta Mater. 68 (2014) 238–253.

[11] K.M. Rahman, N.G. Jones, D. Dye, Micromechanics of twinning in a TWIP steel, Mater. Sci. Eng. A 635 (2015) 133–142.

[12] P. Chowdhury, D. Canadinc, H. Sehitoglu, On deformation behaviour of Fe-Mn based structural alloys, Mater. Sci. Eng. R. Rep. 122 (2017) 1–28.

[13] B. Kim, S.G. Lee, D.W. Kim, Y.H. Jo, J. Bae, S.S. Sohn, S. Lee, Effects of Ni and Cu addition on cryogenic-temperature tensile and Charpy impact properties in austenitic 22Mn-0.45C–1Al steels, J. Alloys Compd. 815 (2020).

[14] D. Li, Y. Feng, S. Song, Q. Liu, Q. Bai, F. Ren, F. Shangguan, Influences of silicon on the work hardening behavior and hot deformation behaviour of Fe–25 wt%Mn–(Si, Al) TWIP steel, J. Alloys Compd. 618 (2015) 768–775.

[15] K.-G. Chin, C.-Y. Kang, S.Y. Shin, S. Hong, S. Lee, H.S. Kim, K.-H. Kim, N.J. Kim, Effects of Al addition on deformation and fracture mechanisms in two high manganese TWIP steels, Mater. Sci. Eng. A 528 (2011) 2922–2928.

[16] R. Kalsar, R.K. Ray, S. Suwas, Effects of alloying addition on deformation mechanisms, microstructure, texture and mechanical properties in Fe-12Mn-0.5C austenitic steel, Mater. Sci. Eng. A 729 (2018) 385–397.

[17] S.M. Lee, I.J. Park, J.G. Jung, Y.K. Lee, The effect of Si on hydrogen embrittlement of Fe-18Mn-0.6C-xSi twinning-induced plasticity steels, Acta Mater. 103 (2016) 264–272.

[18] S.W. Song, J.-N. Kim, H.J. Seo, T. Lee, C.S. Lee, Effects of carbon content on the tensile and fatigue properties in hydrogen-charged Fe-17Mn-xC steels: the opposing trends, Mater. Sci. Eng. A 724 (2018) 469–476.

[19] J. Hufenbach, F. Kochta, H. Wendrock, A. Voß, L. Giebeler, S. Oswald, S. Pilz, U. Kühn, A. Lode, M. Gelinsky, A. Gebert, S and B microalloying of biodegradable Fe-30Mn-1C - effects on microstructure, tensile properties, in vitro degradation and cytotoxicity, Mater. Des. 142 (2018) 22–35.

[20] J.K. Hwang, Effect of copper and aluminum contents on wire drawing behaviour in twinning-induced plasticity steels, Mat. Sci. Eng. A-Struct. 737 (2018) 188–197.

[21] Y.Y. Zhao, J.F. Wang, S. Zhou, X.D. Wang, Effects of rare earth addition on microstructure and mechanical properties of a Fe-15Mn-1.5Al-0.6C TWIP steel, Mat. Sci. Eng. A-Struct. 608 (2014) 106–113.

[22] X. Ma, Z. An, L. Chen, T. Mao, J. Wang, H. Long, X. Hongyan, The effect of rare earth alloying on the hot workability of duplex stainless steel — a study using processing map, Mater. Des. 86 (2015) 848–854.

[23] J. Yang, F. Hao, D. Li, Y. Zhou, X. Ren, Y. Yang, Q. Yang, Effect of RE oxide on growth dynamics of primary austenite grain in hardfacing layer of medium-high carbon steel, J. Rare Earths 30 (2012) 814–819.

[24] A.L. Vidilli, L.B. Otani, W. Wolf, C.S. Kiminami, W.J. Botta, F.G. Coury, C. Bolfarini, Design of a FeMnAlC steel with TWIP effect and evaluation of its tensile and fatigue properties, J. Alloys Compd. 831 (2020).

[25] R.P. Reed, R.E. Schramm, Relationship between stacking-fault energy and x-ray measurements of stacking-fault probability and microstrain, J. Appl. Phys. 45 (1974) 4705–4711.

[26] Z. Wang, C. Song, Y. Zhang, H. Wang, L. Qi, B. Yang, Effects of yttrium addition on grain boundary character distribution and stacking fault probabilities of 90Cu10Ni alloy, Mater. Charact. 151 (2019) 112–118.

[27] X. Tian, Y. Zhang, Effect of Si content on the stacking fault energy in γ-Fe–Mn–Si–C alloys: part I. X-ray diffraction line profile analysis, Mater. Sci. Eng. A 516 (2009) 73–77.

[28] J.K. Hwang, I.H. Son, J.Y. Yoo, A. Zargaran, N.J. Kim, Effect of reduction of area on microstructure and mechanical properties of twinning-induced plasticity steel during wire drawing, Met. Mater. Int. 21 (2015) 815–822.

[29] J.K. Hwang, I.C. Yi, I.H. Son, J.Y. Yoo, B. Kim, A. Zargaran, N.J. Kim, Microstructural evolution and deformation behaviour of twinning-induced plasticity (TWIP) steel during wire drawing, Mat. Sci. Eng. A-Struct. 644 (2015) 41–52.

[30] X. Wang, X. Sun, C. Song, H. Chen, S. Tong, W. Han, F. Pan, Evolution of microstructures and mechanical properties during solution treatment of a Ti–V–Mo-containing high-manganese cryogenic steel, Mater. Charact. 135 (2018) 287–294.

[31] T.R. Jacobs, D.K. Matlock, K.O. Findley, Characterization of localized plastic deformation behaviours associated with dynamic strain aging in pipeline steels using digital image correlation, Int. J. Plast. 123 (2019) 70–85.

[32] I. Jung, S.J. Lee, B.C. De Cooman, Influence of Al on internal friction spectrum of Fe-18Mn-0.6C twinning-induced plasticity steel, Scr. Mater. 66 (2012) 729–732.

[33] Y.L. Cai, S.L. Yang, Y.H. Wang, S.H. Fu, Q.C. Zhang, Characterization of the deformation behaviours associated with the serrated flow of a 5456 Al-based alloy using two orthogonal digital image correlation systems, Mater. Sci. Eng. A 664 (2016) 155–164.

[34] S.J. Lee, J. Kim, S.N. Kane, B.C. De Cooman, On the origin of dynamic strain aging in twinning-induced plasticity steels, Acta Mater. 59 (2011) 6809–6819.

[35] J.K. Kim, B.C. De Cooman, Stacking fault energy and deformation mechanisms in Fe-xMn-0.6C-yAl TWIP steel, Mat. Sci. Eng. A-Struct. 676 (2016) 216–231.

[36] M.C. Jo, M.C. Jo, A. Zargaran, S.S. Sohn, N.J. Kim, S. Lee, Effects of Al addition on tensile properties of partially recrystallized austenitic TRIP/TWIP steels, Mat. Sci. Eng. A-Struct. 806 (2021).

[37] X.Y. Gao, H.P. Ren, H.Y. Wang, S.M. Chen, Effect of lanthanum on the precipitation and dissolution of NbC in micro-alloyed steels, Mat. Sci. Eng. A-Struct. 683 (2017) 116–122.

[38] J. Gao, Y. Huang, D. Guan, A.J. Knowles, L. Ma, D. Dye, W.M. Rainforth, Deformation mechanisms in a metastable beta titanium twinning induced plasticity alloy with high yield strength and high strain hardening rate, Acta Mater. 152 (2018) 301–314.

[39] S.W. Song, Y.J. Kwon, T. Lee, C.S. Lee, Effect of Al addition on low-cycle fatigue properties of hydrogen-charged high-Mn TWIP steels, Mater. Sci. Eng. A 677 (2016) 421–430.

[40] H.K. Yang, Z.J. Zhang, F.Y. Dong, Q.Q. Duan, Z.F. Zhang, Strain rate effects on tensile deformation behaviours for Fe–22Mn–0.6C–(1.5Al) twinning-induced plasticity steel, Mater. Sci. Eng. A 607 (2014) 551–558.

[41] Y.S. Chun, K.-T. Park, C.S. Lee, Delayed static failure of twinning-induced plasticity steels, Scr. Mater. 66 (2012) 960–965.

[42] Y.H. Jo, J. Yang, K.-Y. Doh, W. An, D.W. Kim, H. Sung, D. Lee, H.S. Kim, S.S. Sohn, S. Lee, Analysis of damage-tolerance of TRIP-assisted V10Cr10Fe45Co30Ni5 high-entropy alloy at room and cryogenic temperatures, J. Alloys Compd. 844 (2020).

[43] I. Gutierrez-Urrutia, D. Raabe, Dislocation and twin substructure evolution during strain hardening of an Fe–22wt.% Mn–0.6wt.% C TWIP steel observed by electron channelling contrast imaging, Acta Mater. 59 (2011) 6449–6462.

[44] S. Dancette, L. Delannay, K. Renard, M.A. Melchior, P.J. Jacques, Crystal plasticity modelling of texture development and hardening in TWIP steels, Acta Mater. 60 (2012) 2135–2145.

[45] J. Zhu, J.X. Xie, Z.H. Zhang, H.Y. Huang, Microstructure and Obdurability improvement mechanisms of the La-micro-alloyed H13 steel, Steel Res. Int. 89 (2018).

[46] T.Y. Hsu, Z.Y. Xu, Martensitic transformation in Fe-Mn-Si based alloys, Mat. Sci. Eng. A 273-275 (1999) 494–497.

[47] O.G. B, C. M, A general mechanism of martensitic nucleation: part I. general concepts and the FCC → HCP transformation, Metall. Trans. A. 7 (1976) 1897–1904.

[48] Z. Jiang, P. Wang, D. Li, Y. Li, Effects of rare earth on microstructure and impact toughness of low alloy Cr-Mo-V steels for hydrogenation reactor vessels, J. Mater. Sci. Technol. 45 (2020) 1–14.

[49] H. Liu, P. Fu, H. Liu, Y. Cao, C. Sun, N. Du, D. Li, Effects of rare earth elements on microstructure evolution and mechanical properties of 718H pre-hardened mold steel, J. Mater. Sci. Technol. 50 (2020) 245–256.

[50] A.A. Saleh, C. Haase, E.V. Pereloma, D.A. Molodov, A.A. Gazder, On the evolution and modelling of brass-type texture in cold-rolled twinning-induced plasticity steel, Acta Mater. 70 (2014) 259–271.